

Generalized finite element enrichment functions for discontinuous gradient fields

Alejandro M. Aragón¹, C. Armando Duarte¹, Philippe H. Geubelle^{2,*}

¹ Civil and Environmental Engineering Department, University of Illinois, 205 North Matthews Avenue, Urbana, IL 61801, USA

² Beckman Institute of Advanced Science and Technology, University of Illinois, 405 North Mathews Avenue, Urbana, IL 61801, USA

SUMMARY

A general GFEM/XFEM formulation is presented to solve two-dimensional problems characterized by C^0 continuity with gradient jumps along discrete lines, such as those found in the thermal and structural analysis of heterogeneous materials or in line load problems in homogeneous media. The new enrichment functions presented in this paper allow solving problems with multiple intersecting discontinuity lines, such as those found at triple junctions in polycrystalline materials and in actively cooled microvascular materials with complex embedded networks. We show how the introduction of enrichment functions yields accurate finite element solutions with meshes that do not conform to the geometry of the discontinuity lines. The use of the proposed enrichments in both linear and quadratic approximations is investigated, as well as their combination with interface enrichment functions available in the literature. Through a detailed convergence study, we demonstrate that quadratic approximations do not require any correction to the method to recover optimal convergence rates and that they perform better than linear approximations for the same number of degrees of freedom in the solution of this type of problems. In the linear case, the effectiveness of correction functions proposed in the literature is also investigated.

Copyright © 2008 John Wiley & Sons, Ltd.

KEY WORDS: GFEM; XFEM; Enrichment functions; Poisson equation; Microvascular materials; Polycrystalline microstructure

1. Introduction

Discontinuous gradient fields appear in many problems in physics and engineering. Examples include thermal and structural analyses of heterogeneous materials such as polycrystals, where C^0 continuity is observed along grain boundaries, or composite materials, where a discontinuous gradient is obtained along inclusion boundaries. Homogeneous materials can

*Correspondence to: E-mail address: geubelle@illinois.edu; Tel.: +1 (217) 244-7648; Fax: +1 (217) 244-0720

Contract/grant sponsor: AFOSR MURI; contract/grant number: F49550-05-1-0346

also exhibit solutions characterized by discontinuous gradients. Examples include problems with thermal or structural loads applied over very narrow regions, mathematically modeled as line loads. An example of such a model can be found in the thermal response of a new type of polymeric materials that contains an embedded microvascular network (i.e., a flow network where the diameter of the channels can be as small as $10\text{ }\mu\text{m}$). These materials are currently being considered for thermal management [1]. In the mathematical model of such a system, the cooling effect of the microchannels can be collapsed to a thermal heat sink over a line.

The standard finite element method usually approaches these problems using a conforming finite element mesh [2]. Throughout the paper the terminology *conforming mesh* and *matching mesh* will be used interchangeably, referring to meshes where the edges of the finite elements follow the grain boundaries or the line loads[†]. The inherent C^0 continuous nature of the resulting finite element approximation automatically satisfies the required jumps in the gradient along those boundaries. However, there may be cases where creating a conforming mesh is not feasible or is computationally too demanding. The problem geometry can be such that the creation of a conforming mesh requires finite elements with unacceptable aspect ratios. Furthermore, creating a conforming mesh may necessitate advanced meshing tools not available to the analyst (especially in 3D) or sometimes not sufficiently robust to handle complex geometries. The complexity and computational cost of creating conforming meshes are especially critical in transient problems involving moving line loads or boundaries.

By eliminating the complexity of the computational geometry and allowing the discretization to become independent of the underlying geometry, the Generalized/Extended Finite Element Method (GFEM/XFEM) provides an attractive alternative for this class of problems. Since its introduction in the mid-nineties [3, 4, 5, 6, 7, 8], the method has increasingly gained attention in the FE community because of the added flexibility it offers compared to the conventional FEM. For more details on the history of development of these methods we refer the reader to [9] and the references therein. The GFEM/XFEM allows the use of *a priori* knowledge about the solution of a problem to obtain an improved finite element approximation or to recover optimal convergence by the use of a non-matching mesh. This knowledge is introduced through the use of *enrichment functions* that can range from polynomials to very sophisticated handbook functions (e.g., the Westergaard solutions for a crack in an infinite plate). The mesh independence that the method provides plays a fundamental role in problems that require complete remeshing or even refinement around areas of interest inside the problem domain. Problems addressed by the GFEM include structural problems [10, 11], crack propagation in fracture mechanics [12, 13, 14, 15, 16] and phase interface/change problems [17, 18, 19, 20].

The method has also been used for problems that involve embedded particles or holes [21, 22, 23]. In this line of work, the material interfaces completely cut the finite elements and the proposed enrichment functions attempt to recover the discontinuous gradient field at the interfaces. In order to do so, the elements split by the interfaces are subdivided in integration elements that use the right material properties according to the side of the interfaces they lie on. Material interfaces can also be handled using the GFEM proposed by Babuška and Osborn [24]. They used the so-called broken function to solve 1D problems using finite element meshes that do not match material interfaces. Most of the work available in the literature deals with these

[†]In contrast to other commonly used terminology, where a non-conforming mesh implies, e.g., regions in the mesh having hanging nodes and thus creating a discontinuous solution.

problems, and it was reported that some of these enrichments provide optimal convergence when the mismatch between material properties is not too high [25]. However, little attention has been paid to the more general case where multiple interfaces meet inside a finite element and a C^0 continuous field is recovered. In these cases, a conforming mesh to the junctions could be used in conjunction with the interface enrichment functions mentioned above. Yet, the use of a truly non-conforming mesh is always desired, and two approaches have been proposed in the literature to deal with multiple intersecting weak discontinuities. The first one uses enrichment functions based on the product of the distance functions to the interfaces [26]. The second approach, presented in [27], uses Heaviside enrichments and the continuity is enforced using a traction separation law, following the methodology proposed in [11] for strong discontinuities. This work introduces new enrichment functions that address the problem of having multiple interfaces intersecting inside finite elements and detailed convergence results are given. The end result is the creation of a finite element mesh that is completely independent of the geometry of the problem. The results in this paper are obtained in the context of the heat equation, but the enrichment functions are general and can be used to simulate other physical phenomena (e.g., elasticity problems). It is shown that in all cases, quadratic approximations are more accurate than their linear counterparts for the same number of degrees of freedom. It is also shown that the use of the correction to the GFEM/XFEM proposed in [28] is not required for quadratic approximations in order to achieve optimal convergence rates and that for linear approximations, some enrichment functions fail to recover optimal convergence even when using such correction. A detailed review on the GFEM/XFEM for material modeling can be found in [9].

Section 2 describes the problem to solve and gives a brief introduction to the GFEM. The proposed enrichment functions are presented in Section 3 and convergence results follow in Section 4. Section 5 presents real applications where the proposed enrichment functions are used. Finally, some concluding remarks are given in Section 6.

2. Problem description

Consider in Figure 1 an open domain $\Omega \subset \mathbb{R}^2$ with boundary $\Gamma = \bar{\Omega} - \Omega$, the latter having outward unit normal \mathbf{n} and partitioned into mutually exclusive regions Γ_u and Γ_q such that $\Gamma = \bar{\Gamma}_u \cup \bar{\Gamma}_q$ and $\Gamma_u \cap \Gamma_q = \emptyset$. Dropping the dependance on position \mathbf{x} , the strong form for the steady-state thermal boundary value problem can be written as follows: Given the thermal conductivity $\boldsymbol{\kappa} : \bar{\Omega} \rightarrow \mathbb{R}^2 \times \mathbb{R}^2$, the heat source $f : \Omega \rightarrow \mathbb{R}$, prescribed temperature $t : \Gamma_u \rightarrow \mathbb{R}$ and prescribed heat flux $q : \Gamma_q \rightarrow \mathbb{R}$, find the temperature field $u : \bar{\Omega} \rightarrow \mathbb{R}$ such that

$$\begin{aligned} \nabla \cdot (\boldsymbol{\kappa} \nabla u) + f &= 0 & \text{on } \Omega, \\ u &= t & \text{on } \Gamma_u, \\ \boldsymbol{\kappa} \nabla u \cdot \mathbf{n} &= q & \text{on } \Gamma_q. \end{aligned} \tag{1}$$

Let $\mathcal{U} = \{u \mid u|_{\Gamma_u} = t\} \subset H^1(\bar{\Omega})$ be the set of trial solutions for the temperature field and $\mathcal{V} = \{v \mid v|_{\Gamma_u} = 0\} \subset H_0^1(\bar{\Omega})$ be the variation space. The weak form of the problem reads: Given $\boldsymbol{\kappa}$, f , t and q as before, find $u \in \mathcal{U}$ such that

$$a(w, u) = (w, f) + (w, q)_{\Gamma_q} \quad \forall w \in \mathcal{V}, \tag{2}$$

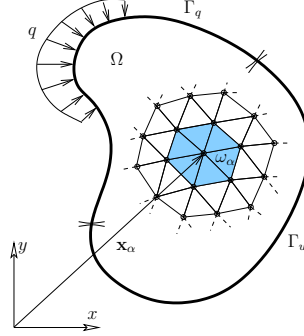


Figure 1: Two-dimensional domain Ω used in the formulation of the problem. The boundary of the domain is split in two mutually exclusive regions Γ_u and Γ_q where Dirichlet and Neumann boundary conditions are applied, respectively. The figure also shows part of a mesh of triangular elements used for discretization showing the cloud or support ω_α for node \mathbf{x}_α .

where the bilinear and linear forms are given by

$$\begin{aligned} a(w, u) &= \int_{\Omega} \nabla w \cdot (\boldsymbol{\kappa} \nabla u) d\Omega, \\ (w, f) &= \int_{\Omega} w f d\Omega, \\ (w, q)_{\Gamma_q} &= \int_{\Gamma_q} w q d\Gamma. \end{aligned}$$

For the Galerkin approximation, let $\mathcal{V}^h \subset \mathcal{V}$ and $\mathcal{U}^h \subset \mathcal{U}$ be finite-dimensional sets such that $\mathcal{V}^h = \{v^h \mid v^h|_{\Gamma_u} = 0\}$ and $\mathcal{U}^h = \{u^h \mid u^h = v^h + t^h, t^h|_{\Gamma_u} \approx t, v^h \in \mathcal{V}^h\}$. The Galerkin statement of the boundary value problem is expressed as: Given $\boldsymbol{\kappa}$, f , t and q as before, find $u^h = v^h + t^h \in \mathcal{U}^h$ such that

$$a(w^h, v^h) = (w^h, f) + (w^h, q)_{\Gamma_q} - a(w^h, t^h) \quad \forall w^h \in \mathcal{V}^h. \quad (3)$$

The application of Dirichlet boundary conditions within the GFEM framework is not straightforward since some enrichment functions may be non-zero at nodes with a prescribed value of the solution. In this work, the penalty method is adopted due to the simplicity in its implementation. The Galerkin form in this context becomes: Given $\boldsymbol{\kappa}$, f , t and q as before, find $u^h \in \mathcal{U}^h$ such that

$$a(w^h, u^h) + \rho (w^h, u^h)_{\Gamma_u} = (w^h, f) + (w^h, q)_{\Gamma_q} + \rho (w^h, t)_{\Gamma_u} \quad \forall w^h \in \mathcal{V}^h, \quad (4)$$

where ρ is a penalty parameter. Dirichlet boundary conditions can also be enforced using Lagrange multipliers [29]. A thorough discussion of these and other methods used to enforce Dirichlet boundary conditions can be found in [30].

Let $\Omega^h \equiv \text{int}(\cup_{\alpha=1}^M \overline{\Omega}_\alpha)$ be a discretization of domain Ω in M finite elements such that $\Omega_\alpha \cap \Omega_\beta = \emptyset \quad \forall \alpha \neq \beta$. Due to discretization error, $\Omega \cong \Omega^h$ and $\Gamma \cong \Gamma^h \equiv \overline{\Omega^h} - \Omega^h$. Let

$\{\mathbf{x}_1, \mathbf{x}_2, \dots, \mathbf{x}_N\}$ be the set of N nodes contained in the discretization and $\varphi_\alpha(\mathbf{x})$ be the standard (Lagrangian) finite element shape function associated with node \mathbf{x}_α . For this node, let $\omega_\alpha \equiv \{\mathbf{x} \mid \varphi_\alpha(\mathbf{x}) \neq 0\}$ be the *cloud* or *support* of \mathbf{x}_α , i.e. the set of all elements attached to it, as illustrated in Figure 1 for a mesh of 3-noded triangular elements. The *partition of unity* property of finite element shape functions specifies that

$$\sum_{\alpha=1}^N \varphi_\alpha = 1, \quad \forall \mathbf{x} \in \overline{\Omega^h}. \quad (5)$$

In the GFEM, the partition of unity property is used to paste together local enrichment functions $\{L_{\alpha i}(\mathbf{x}) : \omega_\alpha \rightarrow \mathbb{R}\}_{i=1}^E$ that aim at representing some localized behavior, with E being the number of enrichment functions used in ω_α . In other words,

$$\psi_{\alpha i} = \varphi_\alpha L_{\alpha i} \quad (\text{no summation on } \alpha). \quad (6)$$

In order to keep the standard finite element shape functions in those elements that contain enriched nodes, we require that $L_{\alpha 0} = 1$, so that a set with E enrichment functions would be $\{1, L_{\alpha i}\}_{i=1}^E$. A temperature approximation using the GFEM thus has the form

$$u^h(\mathbf{x}) = \sum_{\alpha=1}^N \varphi_\alpha(\mathbf{x}) \tilde{U}_\alpha + \sum_{\alpha=1}^N \varphi_\alpha(\mathbf{x}) \sum_{i=1}^E L_{\alpha i}(\mathbf{x}) \hat{U}_{\alpha i}, \quad (7)$$

where the first term corresponds to the standard finite element interpolation and the second term to the enriched/extended part of the approximation, with \tilde{U}_α and $\hat{U}_{\alpha i}$ denoting the standard and enrichment degrees of freedom, respectively. The resulting functions that are used with enriched degrees of freedom can thus be viewed as the cartesian product of the partition of unity shape functions with those of the enrichment set:

$$\{\psi_{\alpha i}\}_{i=0}^E = \varphi_\alpha \times \{1, L_{\alpha i}\}_{i=1}^E. \quad (8)$$

Elements where all nodes are enriched are called *reproducing elements* [28]. These are the elements where enrichment functions have to be used in order to capture some localized behavior. With the exception of a few cases, enrichment functions cannot be used directly as in Equation (8) because problems arise in those elements that do not have all nodes enriched [31, 28]. These elements, located contiguously to the reproducing elements, are called *blending elements*. Optimal convergence is lost due to pathological terms in blending elements unless the enrichment functions are by construction constant or include polynomial enrichments. A correction to the method recently proposed in [28] will be investigated in this work: Given an enrichment function $\psi_{\alpha i}$, let $\psi_{\alpha i}^c$ be the corrected counterpart, defined as

$$\psi_{\alpha i}^c = \psi_{\alpha i} c, \quad (9)$$

where the correction function c over an element is defined as

$$c = \sum_{i \in I^*} \varphi_i, \quad (10)$$

and I^* is the set of all nodes that belong to reproducing elements in the mesh. In other words, c is unity in all reproducing elements (due to the partition of unity property), ramps down in blending elements, and is equally zero elsewhere in the domain. The use of this type of *cut-off*

function can be traced back to [16], in the context of fracture mechanics. An extension of this correction has been studied in [32] for interacting enrichments. Other approaches have been proposed to overcome the problem that arises in blending elements, including using enhanced formulations [31], hierarchical elements [31, 33] and even using Discontinuous Galerkin (DG) formulations [34].

The choice of some enrichment functions can lead to a singular stiffness matrix. Therefore, the resulting system of equations is positive semidefinite and cannot be solved by standard Gauss elimination or Choleski decomposition. In this work, the algorithm described in [10, 35] is used, where a solution vector is obtained by carrying out iterative refinement on the solution of a perturbed problem (ill-conditioned but not singular). The perturbation parameter is chosen as $\varepsilon = 10^{-12}$.

3. Enrichment functions

This section presents the enrichment functions investigated in this work. The objective is to obtain an enrichment function that is continuous and has a discontinuous gradient in the direction perpendicular to the line segments that represent line loads or grain boundaries. The enrichment functions should be general enough so they can be used in the case of a single interface.

3.1. Junction ramp enrichments

Problems where the displacement field is discontinuous (i.e., strong discontinuities) have been addressed in [13, 11, 14]. Most of the enrichment functions for problems with discontinuous field gradients (i.e., weak discontinuities) deal with the case where the discontinuity completely crosses the finite elements [23, 22]. As indicated earlier, for problems with multiple interfaces meeting inside a finite element, enrichment functions based on products of distance functions or Heaviside enrichments have been proposed in [26] and [27], respectively. Here we present other enrichment functions that can be used when dealing with such cases.

Consider the square domain Ω shown in Figure 2. The domain is subdivided in regions $\{\mathcal{G}_i\}_{i=1}^3$ such that $\bar{\Omega} = \cup_{i=1}^3 \bar{\mathcal{G}}_i$. Inner sub-domain boundaries are defined as $\Gamma_{ij} \equiv \bar{\mathcal{G}}_i \cap \bar{\mathcal{G}}_j, i \neq j$ and the junction coordinate as $\mathbf{x}_J = \cap_{i,j=1, i \neq j}^3 \bar{\Gamma}_{ij}$. In the case of a polycrystalline microstructure, a region \mathcal{G}_i represents one of the grains in the domain whereas Γ_{ij} represents the material interface between grains i and j . In the case of a homogeneous material, the sub-domain boundaries Γ_{ij} can be viewed as line loads. These line loads become heat sinks in the case of the microvascular material alluded to in Section 1.

The first enrichment considers each sub-domain individually and can be obtained by integrating the enrichment functions proposed for strong discontinuities in polycrystalline materials [11], in the direction perpendicular to the material interfaces (or line loads). For a particular sub-domain, the function ramps only inside it and it is constant elsewhere. For sub-domain \mathcal{G}_i , the ramp enrichment function is

$$r_i(\mathbf{x}) = \begin{cases} 1 + \min_{i=1}^n d_i(\mathbf{x}) & \text{if } \mathbf{x} \in \mathcal{G}_i, \\ 1 & \text{otherwise,} \end{cases} \quad (11)$$

where $d_i(\mathbf{x})$ is the distance function to the i -th line segment representing one of the n

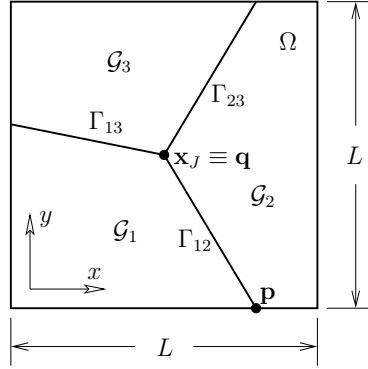


Figure 2: A 2D square domain $\Omega \equiv L \times L$ is divided in regions $\{\mathcal{G}_i\}_{i=1}^3$ such that $\overline{\Omega} = \cup_{i=1}^3 \overline{\mathcal{G}_i}$. Each sub-domain can be viewed as different grains in the case of a polycrystalline microstructure. In the case of a homogeneous material, inner boundaries can be viewed as line loads (heat sinks in the case of a microvascular material for active cooling applications).

inner boundaries of \mathcal{G}_i and the unity constant is introduced so that the resulting matrix is better conditioned. This means that we might need to consider as many enrichment functions as sub-domains. In [11], it was found that for n intersecting inner boundaries, considering $n - 1$ enrichments was enough due to the fact that one of the enrichments could be obtained as a linear combination of the others. This issue will be investigated shortly for the type of enrichment functions used in this work. Schematics showing the convention adopted to represent the enrichment function are illustrated in Figure 3 for the three sub-domain problem, showing that for each enrichment the function is non-constant in its shaded area. Arrows in the schematic figures indicate the direction where the ramp function increases in magnitude whereas dashed lines indicate bisector lines between adjacent line segments. The function is C^0 continuous along the bisector lines so they are also considered when subdividing the element for integration purposes, as explained in Section 4.3.

A second option that involves less degrees of freedom can be obtained by combining the enrichment functions defined in Equation (11) into a single junction ramp enrichment $R(\mathbf{x})$. For a junction \mathbf{x}_J between m grains with n boundaries Γ_{ij} , the enrichment function is defined as

$$R(\mathbf{x}) = \sum_{i=1}^m r_i(\mathbf{x}) - m = \min_{i=1}^n d_i(\mathbf{x}). \quad (12)$$

The enrichment function is obtained by computing the distance from point \mathbf{x} to the closest line in the domain. This function is illustrated in Figure 4, both in 3D and its equivalent planar representation. Note that, when there is a single line segment (e.g., single material interface), the enrichment function reduces to the enrichment proposed in [22].

The distance function to the i -th line can be computed analytically as follows: the closest point lying on the ray having the same slope as the line segment defined by points \mathbf{p} and

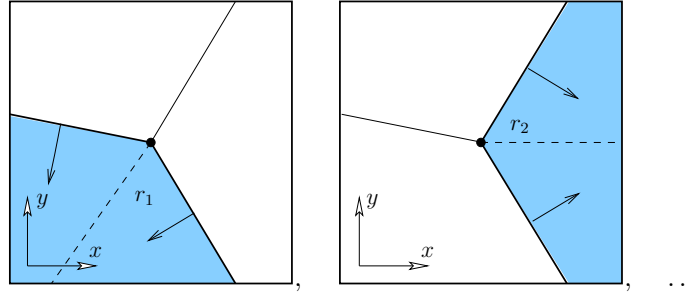


Figure 3: Ramp enrichments given by Equation (11), non-constant on their respective shaded area. Arrows denote the direction where the ramps increase in magnitude. Bisector lines are shown as dashed lines.

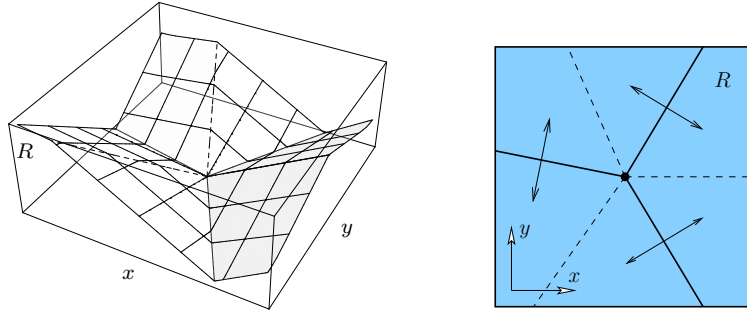


Figure 4: Single junction ramp enrichment $R(\mathbf{x})$ showing a 3D representation (left) and its equivalent 2D schematic (right).

$\mathbf{q} \equiv \mathbf{x}_J$ (see Figure 2) is $\mathbf{x}^* = \mathbf{p} + s(\mathbf{x})(\mathbf{q} - \mathbf{p})$, with

$$s(\mathbf{x}) = \frac{(\mathbf{x} - \mathbf{p}) \cdot (\mathbf{q} - \mathbf{p})}{\|\mathbf{q} - \mathbf{p}\|^2}.$$

Then, the distance function is given by

$$d_i(\mathbf{x}) = \begin{cases} \|\mathbf{x} - \mathbf{p}\| & \text{if } s(\mathbf{x}) \leq 0, \\ \|\mathbf{x} - \mathbf{q}\| & \text{if } s(\mathbf{x}) \geq 1, \\ \|\mathbf{p} + s(\mathbf{x})(\mathbf{q} - \mathbf{p}) - \mathbf{x}\| & \text{otherwise.} \end{cases} \quad (13)$$

When the closest point on the line segment is obtained through an orthogonal projection (i.e., $0 \leq s(\mathbf{x}) \leq 1$), we approximate the distance function to the i -th line segment by using the level set method [36, 26], such that

$$d_i^h(\mathbf{x}) = \left| \sum_j \varphi_j(\mathbf{x}) \Lambda_j^i \right|, \quad (14)$$

where Λ_j^i is the level set function value at the j -th node of the element that contains point \mathbf{x} .

Polynomial functions can also be used together with the ramp functions presented. For a quadratic finite element approximation, we enrich each node $\mathbf{x}_\alpha = (x_\alpha, y_\alpha)$ in the mesh with linear polynomials

$$\xi = \frac{x - x_\alpha}{h_\alpha}, \quad \eta = \frac{y - y_\alpha}{h_\alpha}, \quad (15)$$

where h_α is a scaling parameter related to the size of the cloud of node \mathbf{x}_α . The ramp functions are also multiplied by the polynomial enrichments defined in Equation (15), so when using, e.g., the single ramp enrichment R the enrichment functions on node \mathbf{x}_α become

$$\mathcal{L} = \{1, \xi, \eta\} \times \{1, R\} = \{1, \xi, \eta, R, \xi R, \eta R\}. \quad (16)$$

These high-order enrichment functions follow the same concept as those proposed in [37, 38].

The aforementioned enrichment functions r_i and R defined in Equations (11) and (12), respectively, are used to enrich all nodes whose support intersect any of their sub-domain boundaries. However, there are situations where the required information to produce these enrichments is not easily available. The information about the intersecting lines can be obtained locally when evaluating the junction even if the complete geometric description of the sub-domains is not available. The proposed enrichments can still be applied to the finite element nodes with support interacting with the junction. Other nodes of elements completely split by the interfaces can be enriched with other interface enrichments, thus allowing the mixing of the enrichments proposed here with other enrichment functions available in the literature. Figure 5 shows schematically the mixing between interface and junction enrichments. The nodes of elements that are completely cut by the sub-domain inner boundaries are enriched with interface enrichments unless they already have a junction enrichment (see Figure 5b). The convention used to denote the set of enrichment functions used at a node when mixing types is

$$\mathcal{L} = \left\{ 1, \left[\{L_{\alpha i}^I(\mathbf{x})\}_{i=1}^{E_I} \mid \{L_{\alpha i}^J(\mathbf{x})\}_{i=1}^{E_J} \right] \right\}, \quad (17)$$

where E_I and E_J represent the number of enrichment functions used for *interfaces* and *junctions*, respectively, and $[\cdot \mid \cdot]$ denotes one set of enrichments or the other, but not both. For example, the enrichment set $\mathcal{L} = \{1, \xi, \eta\} \times \{1, [M|R]\}$ is equivalent to

$$\mathcal{L} = \left\{ 1, \xi, \eta, \left[\{L_{\alpha i}^I\}_{i=1}^3 \mid \{L_{\alpha i}^J\}_{i=1}^3 \right] \right\} = \{1, \xi, \eta, [M, M\xi, M\eta \mid R, R\xi, R\eta]\},$$

where $\{L_{\alpha i}^I\}_{i=1}^3 = \{M, M\xi, M\eta\}$ and $\{L_{\alpha i}^J\}_{i=1}^3 = \{R, R\xi, R\eta\}$ denote the sets of enrichment functions used for interfaces and junctions, respectively. The nodes of the element that contains the junction are enriched with the functions described above. As a result, the junction function is non-zero over $\Omega^L \equiv \omega_\alpha \cup \omega_\beta \cup \omega_\gamma$. Thus, we use a unique enrichment function that ramps in all directions inside Ω^L (Figure 6b) or single ramp enrichments for each pair of adjacent lines considering them as part of a fictitious sub-domain (Figure 6a). This approach also allows us to combine the junction enrichments proposed above with other interface enrichments available in the literature.

The correction proposed by Fries [28] may be used in conjunction with the proposed enrichments. The corrected enrichment functions require an additional layer of nodes to be enriched, thus increasing the size of the support of the function and consequently the number of degrees of freedom. In other words, not only the nodes of elements that interact with inner

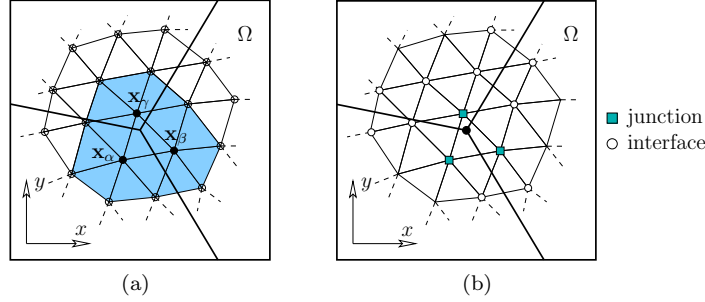


Figure 5: Mixing between interface and junction enrichments. (a) Area $\Omega^L \equiv \omega_\alpha \cup \omega_\beta \cup \omega_\gamma$ (shaded area) where the junction function is applied. (b) Choice of interface and junction enrichments.

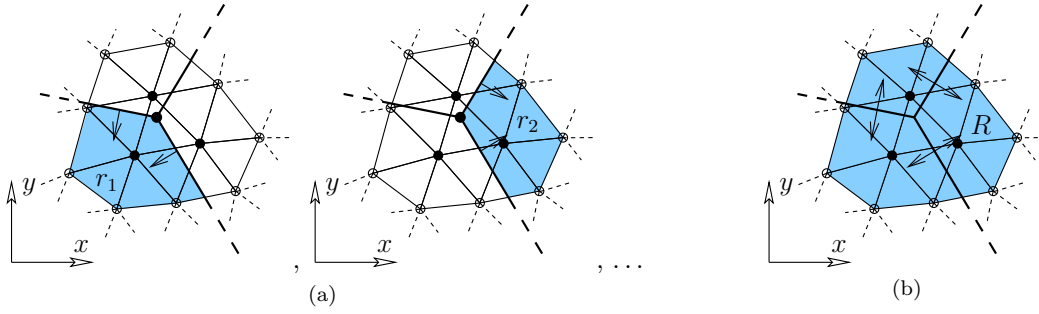


Figure 6: Junction enrichment functions applied only to those nodes with support interacting with the junction \mathbf{x}_J . This approach is appealing for problems where the complete geometry of the sub-domains cannot be defined easily or when mixing enrichment types. (a) $r_1, r_2, \dots \forall \mathbf{x} \in \Omega^L$; (b) $R \forall \mathbf{x} \in \Omega^L$.

boundaries are enriched but also those of contiguous elements (i.e., blending elements). The functions, taking into account the correction, are denoted hereafter as r_i^c and R^c .

3.2. Interface enrichments

Interface enrichments have been investigated primarily for inclusions and voids inside another material. Even though many examples in this work do not have a material interface per se, these functions are still referred to as *interface enrichments* to be consistent with the existing literature. These functions can be used to enrich the nodes of elements that are completely cut by the lines, unless they are enriched with junction ramp enrichments r_i or R or their corrected counterparts.

Ridge enrichment Introduced by Möes et al. [23], the ridge enrichment function is given by

$$M(\mathbf{x}) = \sum_i^N |\Lambda_i| \varphi_i(\mathbf{x}) - \left| \sum_i^N \Lambda_i \varphi_i(\mathbf{x}) \right|, \quad (18)$$

where Λ_i is the level set function value corresponding to the i -th node. This function constructs a continuous field inside the element with a ridge following the path of the interface. By construction, this enrichment function is identically zero in elements that do not contain the interface. As a result, no problems arise in blending elements and the correction given by Equation (10) is not necessary.

Ramp enrichments These functions are a special case of the ramp enrichments presented before when considering a single line segment. The function R ramps in both perpendicular directions from the line segment that represents the inner boundary. This function was proposed by Sukumar et al. in [22] with special treatment on blending elements. Chessa et al. made use of this function for solidification problems [39]. Fries [28] used this function together with his proposed correction and showed optimal convergence rates in the case of a circular inclusion for 2D elasto-statics. In this work the latter is denoted R^c . Similarly, the functions $r_i, i = 1, 2$ and their corrected counterparts introduced before can be used for interface enrichments when considering a single line segment. These enrichment functions ramp to one side of the line segment and are constant on the other side. A single ramp function on one side of the interface was used in [40] for a comparison between the XFEM and the Immerse Interface Method.

4. Convergence results

Convergence results for all enrichment functions investigated are presented in this section.

4.1. Single uniform heat source

This example is used to introduce the enrichment functions used in this work in the context of a single line load. Let the temperature field over $\Omega \equiv L \times L$ (Figure 7) be defined as

$$u(x, y) = \begin{cases} \frac{x(L-4x)(5L-4x)(L-2x)}{6L^3} & x \leq L/2, \\ \frac{(3L-4x)(L-2x)(L-x)(L+4x)}{6L^3} & x \geq L/2. \end{cases} \quad (19)$$

This function, which is constant in the y direction, was manufactured from two polynomials $X_1(x)$ and $X_2(x)$ at each side of the line $x = L/2$ such that $\llbracket u'(L/2) \rrbracket = -1$. This constant jump along the line $x = L/2$ can be clearly seen in Figure 8. The body heat source term that needs to be applied to all elements results from substituting Equation (19) in the differential equation:

$$f_b(x, y) = \frac{-102L^4 + 576L^3x - 576L^2x^2}{9L^5}. \quad (20)$$

For the finite element solutions, the domain Ω^h is then discretized using matching (M) and non-matching (NM) meshes. A single line heat source of unit magnitude per unit length traverses the domain. This line load is the responsible for creating the jump $\llbracket u'(L/2) \rrbracket = -1$. Recall

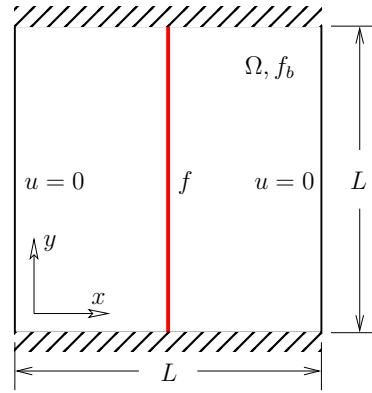


Figure 7: Schematic for the single uniform line heat source. A 2D square domain $\Omega = L \times L$ contains a single line heat source f that traverses it from side to side and a body heat source f_b . Boundary conditions include prescribed temperature $u = 0$ at left and right edges, and insulated bottom and top edges.

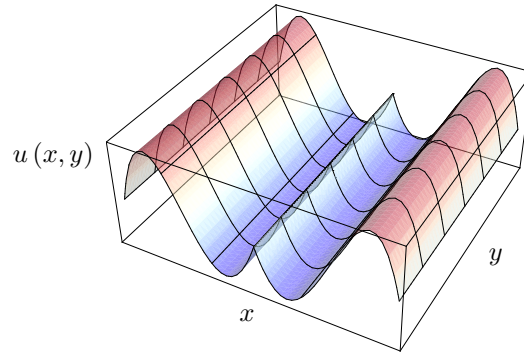


Figure 8: Temperature distribution given by Equation (19) showing the constant jump in the derivative at $x = L/2$.

that by a matching mesh we mean that the heat source follows the edges of the finite elements. Top and bottom edges are insulated (i.e., $q = 0$) and a temperature $t = 0$ is prescribed at left and right edges. The Dirichlet boundary conditions are enforced using the penalty method because the example involves the use of the polynomial enrichments given by Equation (15).

The results from the convergence study for this problem are illustrated in Figures 9 and 10 for the L_2 and energy norms, respectively. Figures on the top show in abscissas the number of degrees of freedom n whereas the figures on the bottom show the mesh size h . The error in

	$h - E$	$h - L_2$	$n - E$	$n - L_2$
linear FEM-M	1	2	0.5	1
quadratic FEM-M	2	3	1	1.51
linear FEM-NM	0.54	1.58	0.27	0.79
$\mathcal{L}_1 = \{1, M\}$	1	2.02	0.51	1.04
$\mathcal{L}_2 = \{1, r_1\}$	0.53	1.57	0.27	0.8
$\mathcal{L}_3 = \{1, r_1^c\}$	1	2	0.51	1.02
$\mathcal{L}_4 = \{1, r_1, r_2\}$	0.53	1.58	0.27	0.8
$\mathcal{L}_5 = \{1, r_1^c, r_2^c\}$	0.99	2	0.51	1.04
$\mathcal{L}_6 = \{1, R\}$	0.53	1.57	0.27	0.79
$\mathcal{L}_7 = \{1, R^c\}$	0.56	1.62	0.29	0.83
$\mathcal{L}_8 = \{1, \xi, \eta\} \times \{1, M\}$	2	3	1.02	1.52
$\mathcal{L}_9 = \{1, \xi, \eta\} \times \{1, r_1\}$	1.93	2.93	0.98	1.49
$\mathcal{L}_{10} = \{1, \xi, \eta\} \times \{1, r_1, r_2\}$	1.97	2.96	1	1.51
$\mathcal{L}_{11} = \{1, \xi, \eta\} \times \{1, R\}$	2	2.98	1.01	1.51

Table I: Convergence rates for the single uniform heat source example. All convergence rates reported are obtained using the two most refined solutions.

the L_2 is given by

$$\|u - u^h\|_{L_2(\Omega)} \equiv \sqrt{\int_{\Omega} (u - u^h)^2 d\Omega},$$

whereas the error in the energy norm is

$$\|u - u^h\|_{E(\Omega)} \equiv \sqrt{\|u - u^h\|_{L_2(\Omega)}^2 + \int_{\Omega} \|\nabla u - \nabla u^h\|^2 d\Omega}.$$

Our reference solutions are the standard finite element solutions on matching meshes, denoted as FEM-M in Figures 9 and 10. The linear FEM-M, obtained with standard 3-noded elements, attains optimal convergence of 2 in the L_2 norm and 1 in the energy norm with respect to the mesh size h . 6-noded elements are used in the quadratic FEM-M, and optimal convergence rates of 3 and 2 are obtained. Refer to Table I for a complete list of convergence values. The FEM-NM solutions refer to those of non-matching meshes without the use of enrichment functions. The purpose of showing these solutions is two-fold: Firstly, this solution establishes an upper bound on the error of other solutions. Secondly, even though the convergence rate is very poor when compared to other solutions, the standard FEM still converges as the meshes are refined because the interface is contained in increasingly smaller elements. The curve $\mathcal{L}_1 = \{1, M\}$ corresponds to the use of the ridge function proposed in [23], showing optimal performance for this problem. All ramp enrichment functions without the correction proposed in [28] perform as poorly as the FEM-NM. Adding the correction enables them to recover optimal convergence rates for all ramp functions but the one that ramps to both sides of the interface (i.e., R^c). For the quadratic approximations using enrichments, all nodes in the mesh are enriched with the linear polynomials given by Equation (15). As explained before, the discontinuous part of the approximation is also multiplied by polynomials so the enrichment functions are given by Equation (16). The results show that quadratic optimal convergence is

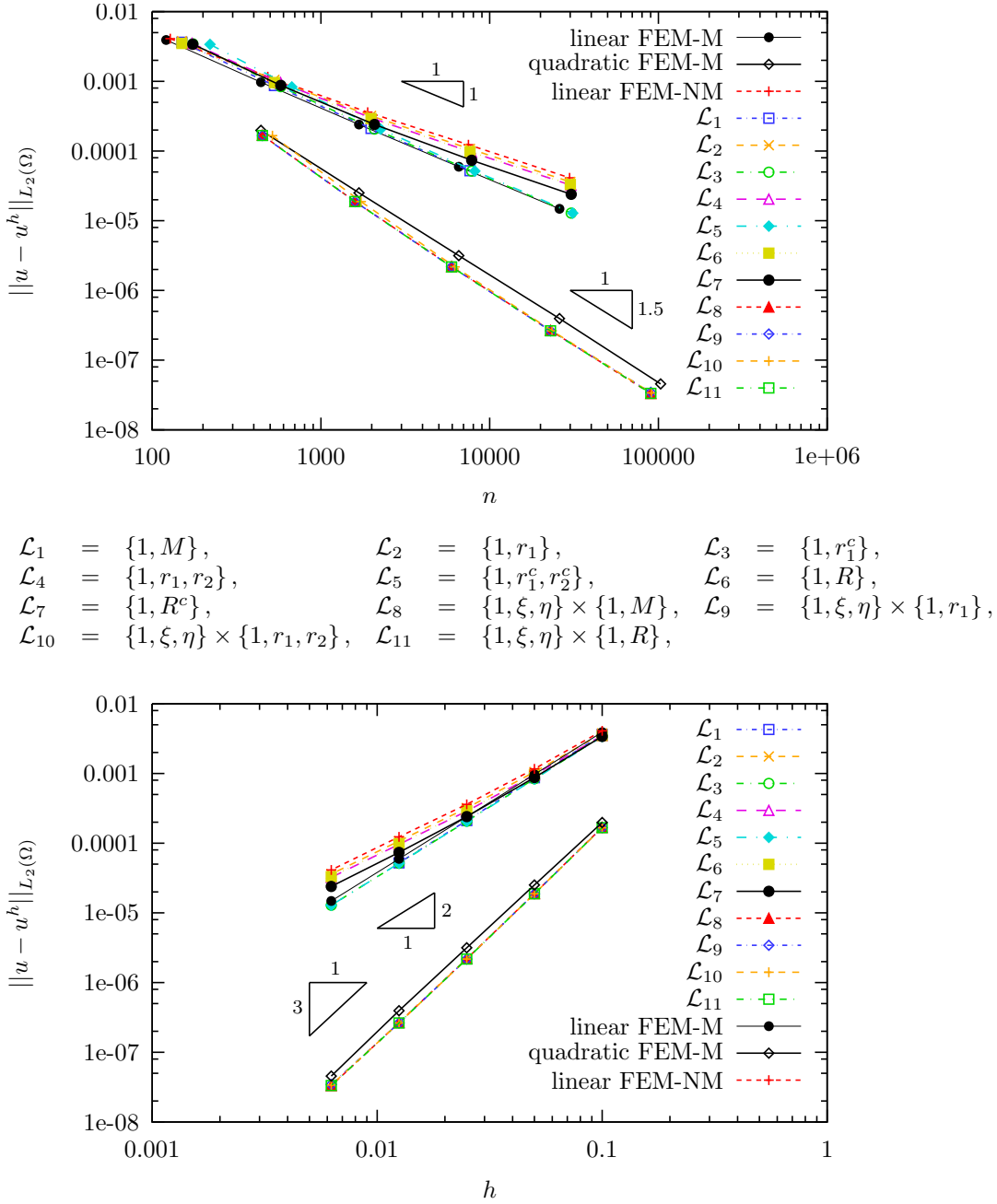
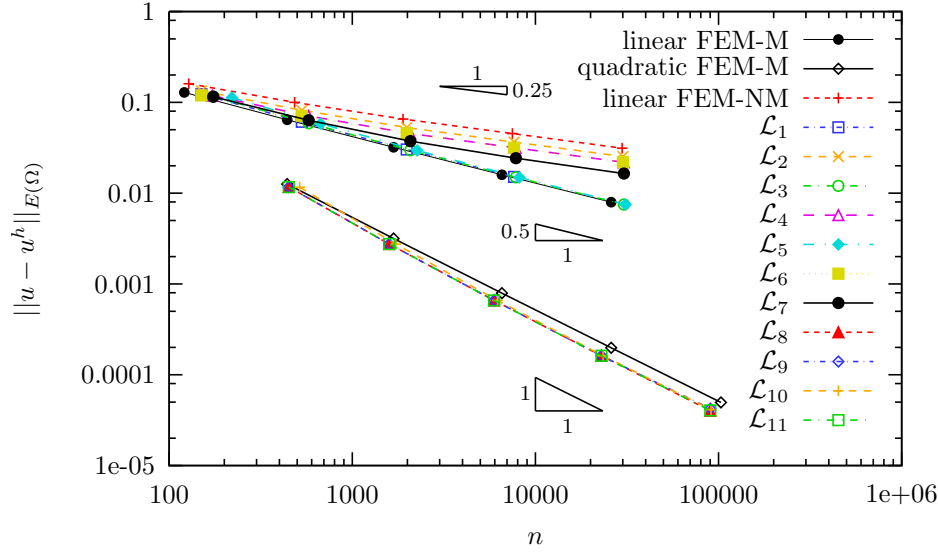


Figure 9: Convergence results in the L_2 norm for the single uniform heat source example shown in Figure 7. The top figure shows in abscissas the number of degrees of freedom n whereas the bottom figure shows the mesh size h .



$$\begin{aligned}
 \mathcal{L}_1 &= \{1, M\}, & \mathcal{L}_2 &= \{1, r_1\}, & \mathcal{L}_3 &= \{1, r_1^c\}, \\
 \mathcal{L}_4 &= \{1, r_1, r_2\}, & \mathcal{L}_5 &= \{1, r_1^c, r_2^c\}, & \mathcal{L}_6 &= \{1, R\}, \\
 \mathcal{L}_7 &= \{1, R^c\}, & \mathcal{L}_8 &= \{1, \xi, \eta\} \times \{1, M\}, & \mathcal{L}_9 &= \{1, \xi, \eta\} \times \{1, r_1\}, \\
 \mathcal{L}_{10} &= \{1, \xi, \eta\} \times \{1, r_1, r_2\}, & \mathcal{L}_{11} &= \{1, \xi, \eta\} \times \{1, R\},
 \end{aligned}$$

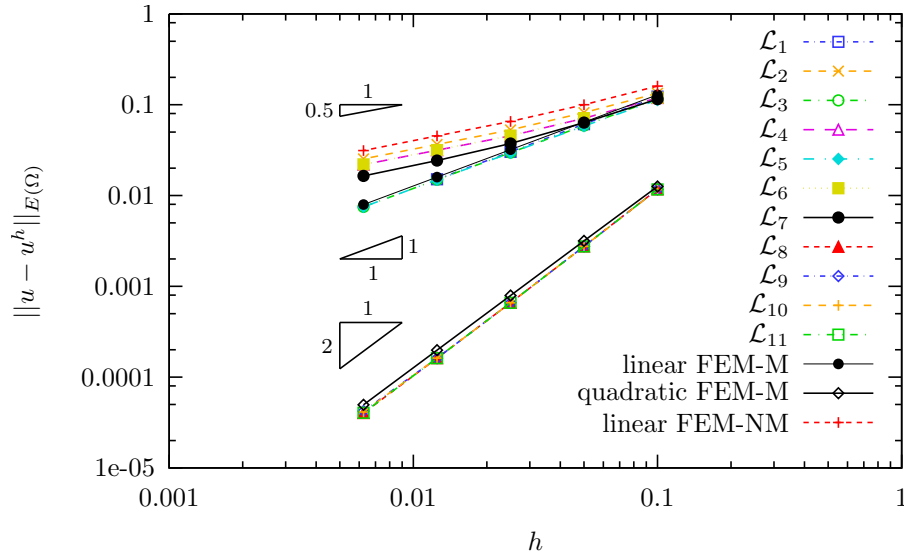


Figure 10: Convergence results in the energy norm for the single uniform heat source example shown in Figure 7. The top figure shows in abscissas the number of degrees of freedom n whereas the bottom figure shows the mesh size h .

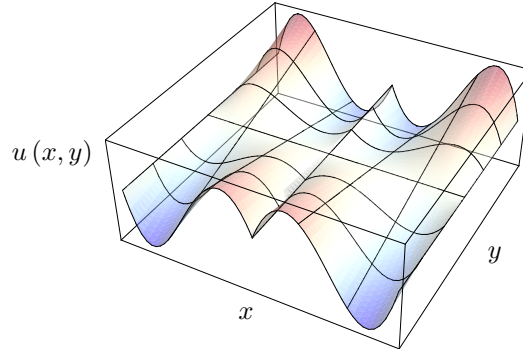


Figure 11: Temperature distribution given by Equation (21) showing the linear jump in the derivative at $x = L/2$.

obtained in all cases, without the use of Fries' correction term and regardless of the enrichment used. Note also that all approximations using enrichment functions are more accurate than the quadratic standard FE approximation on matching meshes. Furthermore, for any given number of degrees of freedom n , quadratic approximations are more accurate than the linear approximations. Therefore, quadratic approximations should be preferred over linear ones, even for very coarse finite element meshes when solving this class of problems.

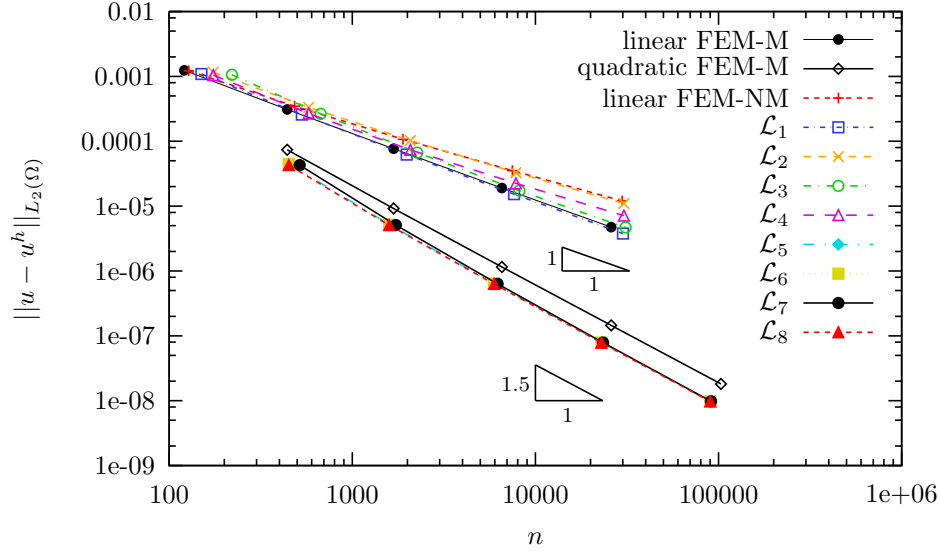
4.2. Single linearly varying heat source

There might be cases where the jump in the derivative of the solution is not constant but spatially varying. To investigate this situation we multiply the temperature field from the previous example by $Y(y) = y - L/2$, which results in a field that has a linearly varying jump in the derivative along the line load (i.e., $\llbracket u_{,x}(L/2, y) \rrbracket = -Y(y)$). The temperature field is then

$$u(x, y) = \begin{cases} \frac{x(L-4x)(5L-4x)(L-2x)(2y-L)}{12L^3} & x \leq L/2, \\ \frac{(3L-4x)(L-2x)(L-x)(L+4x)(2y-L)}{12L^3} & x \geq L/2. \end{cases} \quad (21)$$

and again it is shown in Figure 11. The body source applied to all elements in the discretization is the same as that given by Equation (20). Left and right edges are Dirichlet boundaries again using the penalty method. Top and bottom edges this time have a prescribed heat flux ($q = u_{,y}$ for the top edge and $q = -u_{,y}$ for the bottom edge).

The convergence results for this example are shown in Figures 12 and 13, where non-optimal enrichment functions from the previous example were excluded. The results show that the corrected ramp enrichments used previously do not achieve optimal convergence anymore. Therefore, the corrected ramp functions can only represent a constant jump, which is clear because the nature of the function. In other words, the function has along the line a constant jump in the derivative normal to the line so a linear variation is not possible. However, using the ramp functions with linear polynomial enrichments brings optimal convergence back, as shown in the figure for the quadratic approximations. Interestingly, the ridge enrichment function performs as well as before. This ridge function, which is not constant over the ridge, performs



$$\begin{aligned}
 \mathcal{L}_1 &= \{1, M\}, & \mathcal{L}_2 &= \{1, r_1^c\}, & \mathcal{L}_3 &= \{1, r_1^c, r_2^c\}, \\
 \mathcal{L}_4 &= \{1, R^c\}, & \mathcal{L}_5 &= \{1, \xi, \eta\} \times \{1, M\}, & \mathcal{L}_6 &= \{1, \xi, \eta\} \times \{1, r_1\}, \\
 \mathcal{L}_7 &= \{1, \xi, \eta\} \times \{1, r_1, r_2\}, & \mathcal{L}_8 &= \{1, \xi, \eta\} \times \{1, R\},
 \end{aligned}$$

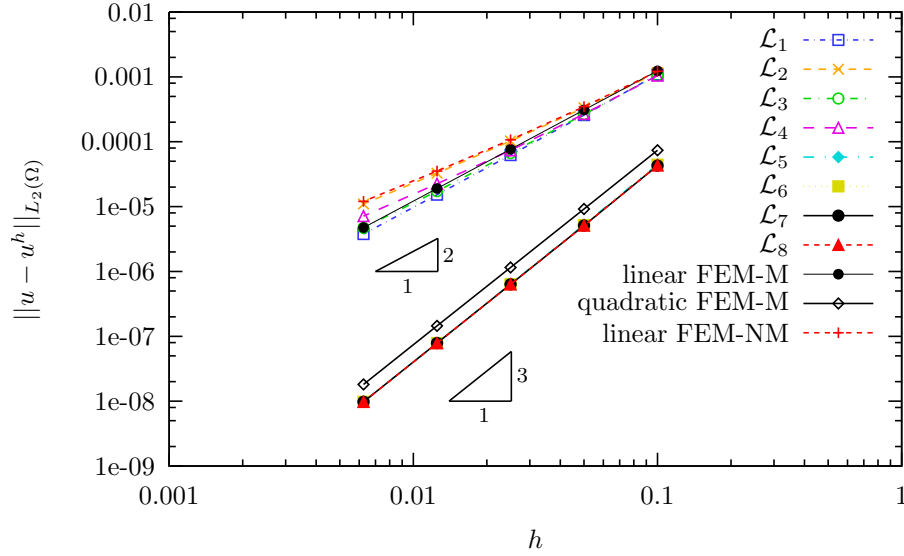


Figure 12: Convergence results in the L_2 norm for the linearly varying heat source example. Top and bottom figures show in abscissas the number of degrees of freedom n and the mesh size h , respectively.

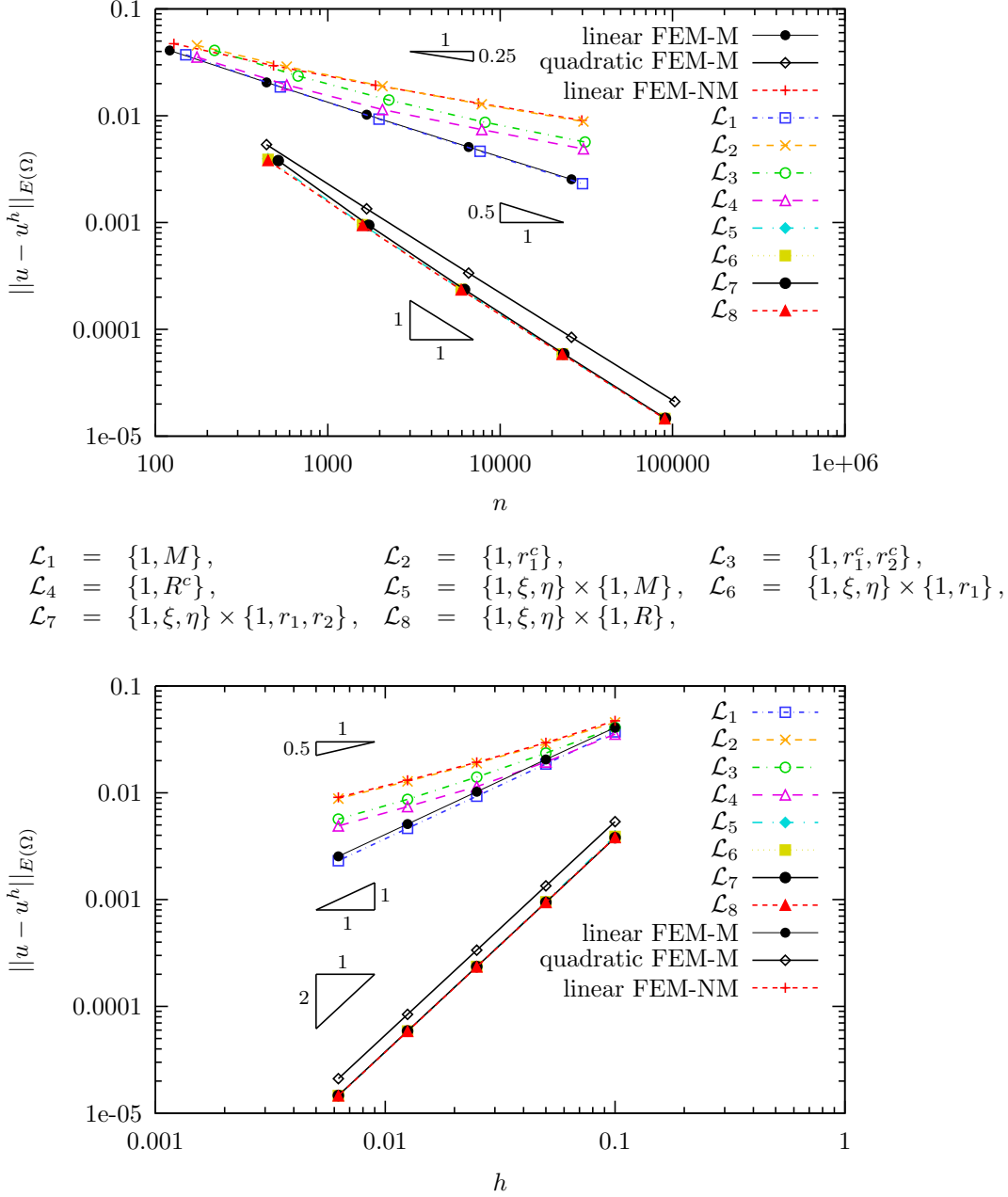


Figure 13: Convergence results in the energy norm for the linearly varying heat source example. Top and bottom figures show in abscissas the number of degrees of freedom n and the mesh size h , respectively.

	$h - E$	$h - L_2$	$n - E$	$n - L_2$
linear FEM-M	1	2.01	0.51	1.01
quadratic FEM-M	2	3	1	1.5
linear FEM-NM	0.53	1.55	0.27	0.78
$\mathcal{L}_1 = \{1, M\}$	1	2.02	0.51	1.02
$\mathcal{L}_2 = \{1, r_1^c\}$	0.53	1.58	0.27	0.81
$\mathcal{L}_3 = \{1, r_1^c, r_2^c\}$	0.61	1.88	0.32	0.98
$\mathcal{L}_4 = \{1, R^c\}$	0.6	1.66	0.31	0.85
$\mathcal{L}_5 = \{1, \xi, \eta\} \times \{1, M\}$	2.01	3.01	1.02	1.53
$\mathcal{L}_6 = \{1, \xi, \eta\} \times \{1, r_1\}$	2.01	3.01	1.02	1.53
$\mathcal{L}_7 = \{1, \xi, \eta\} \times \{1, r_1, r_2\}$	2	3.01	1.02	1.53
$\mathcal{L}_8 = \{1, \xi, \eta\} \times \{1, R\}$	2.01	3.01	1.02	1.52

Table II: Convergence rates for the linearly varying heat source example. All convergence rates reported are obtained using the two most refined solutions.

better than the ramp functions when the jump is not constant. Furthermore, no correction is needed since the function is already zero in blending elements. As a result, this function uses less degrees of freedom than the ramps for linear approximations and should be used when possible. For quadratic approximations, the ramp functions perform as well as the ridge function, and they have the same number of degrees of freedom (except when using two single-sided ramps). Table II lists all convergence rates obtained in this example.

4.3. Multiple uniform heat sources

The same domain Ω used in the previous examples is used here. The problem now contains three line heat sources of unit magnitude per unit length that meet at the center of the domain, as illustrated in Figure 14. An exact solution for this problem is not available so convergence rates will be measured with respect to an energy value obtained using a cubic approximation on a very fine matching mesh (10-node triangles). The error in the energy norm is computed as

$$\|u - u^h\|_{E(\Omega)} \equiv \sqrt{a(u, u) - a(u^h, u^h)}. \quad (22)$$

The boundary conditions for this example include prescribed temperature along the right edge whereas all other edges are insulated.

Figure 15 shows typical integration meshes used in this example when neglecting and considering bisector lines. In the latter case, the bisector lines are considered in addition to the lines that define the heat sources for the initial element subdivision into integration elements. Thus, the resulting partitioned elements that lie along bisector directions are forced to have their edges aligned with the bisector lines. During the computation of local matrices and vectors, elements are created in places where the functions are not smooth and therefore difficult to integrate. This can be seen in Figure 15a, where not considering bisector lines for the initial partitioning has created smaller integration elements along the bisector directions. Thus, this technique can be used together with the GFEM to find regions of difficult integration inside the mesh. The algorithm used in this work uses adaptive integration only in elements with enriched nodes. No adaptive integration is used in the rest of the mesh since in those elements

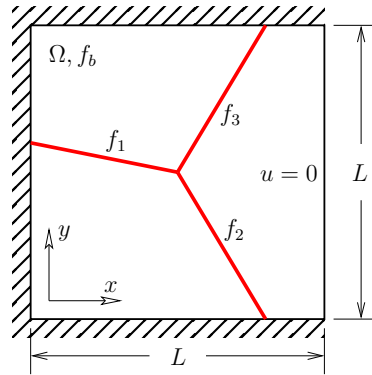


Figure 14: Geometry of test problem with multiple uniform line heat sources. A 2D square domain Ω of side L contains uniform heat sources f_i , $(i = 1, 2, 3)$ that meet at the center of the domain. Boundary conditions include prescribed temperature $u = 0$ at the right edge whereas the remaining edges are insulated.

a standard finite element approximation is used (as long as no polynomial enrichments are used). Moreover, a single level of recursion is used in blending elements because the enrichment function in those elements is smooth. Adding bisector lines reduces dramatically the level of recursion used in elements that lie in the path of bisector lines, as noted in Figure 15b. The use of this technique within the GFEM framework is not new and can be traced back to [41, 21].

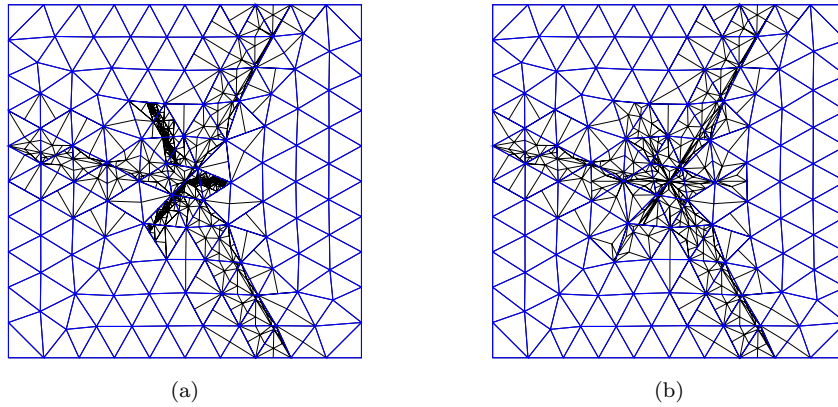
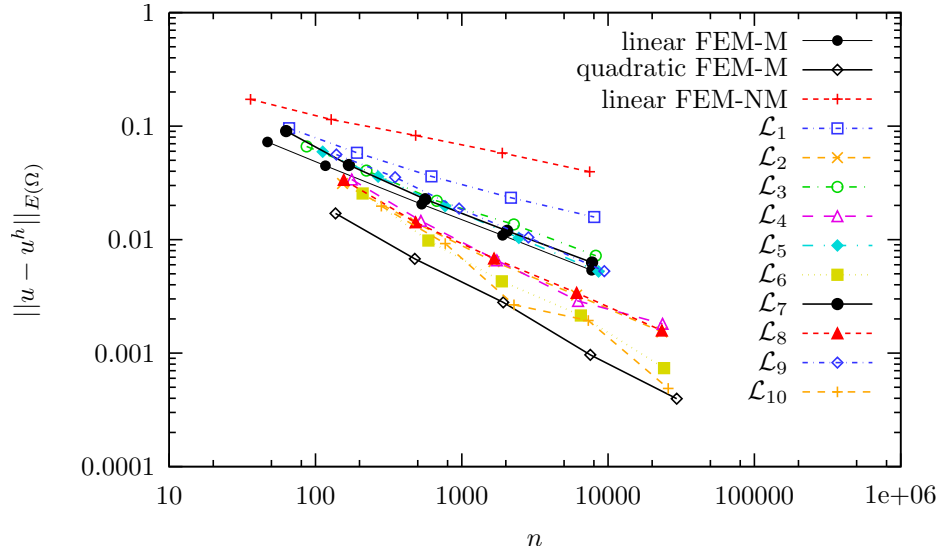


Figure 15: Resulting integration mesh using adaptive numerical quadrature. (a) Bisector lines not considered; (b) Bisector lines considered.

Convergence results for this problem are summarized in Figure 16. As in the previous examples, FEM-M and FEM-NM denote the standard finite element solutions on matching



$$\begin{aligned}
 \mathcal{L}_1 &= \{1, R^c\}, & \mathcal{L}_2 &= \{1, \xi, \eta\} \times \{1, R\}, \\
 \mathcal{L}_3 &= \{1, r_1^c, r_2^c\}, & \mathcal{L}_4 &= \{1, \xi, \eta\} \times \{1, r_1, r_2\}, \\
 \mathcal{L}_5 &= \{1, r_1^c, r_2^c, r_3^c\}, & \mathcal{L}_6 &= \{1, \xi, \eta\} \times \{1, r_1, r_2, r_3\}, \\
 \mathcal{L}_7 &= \{1, [M|R^c]\}, & \mathcal{L}_8 &= \{1, \xi, \eta\} \times \{1, [M|R]\}, \\
 \mathcal{L}_9 &= \{1, [M|r_1^c, r_2^c, r_3^c]\}, & \mathcal{L}_{10} &= \{1, \xi, \eta\} \times \{1, [M|r_1, r_2, r_3]\},
 \end{aligned}$$

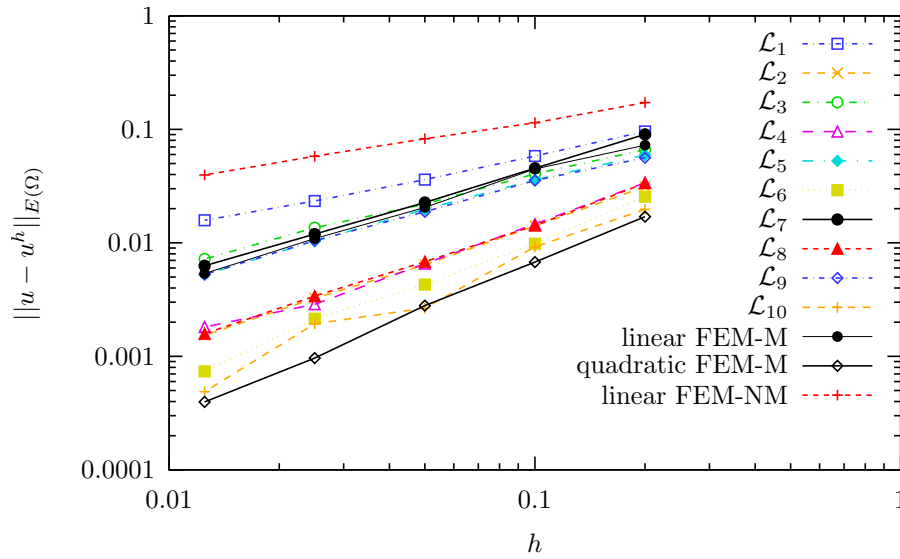


Figure 16: Convergence results in the energy norm for the multiple heat sources example. The top figure shows in abscissas the number of degrees of freedom n whereas the bottom figure shows the mesh size h .

and non-matching meshes, respectively. The figure shows that the second junction enrichment proposed (i.e., R^c) performs sub-optimally for a linear approximation. Having a unique function does not provide enough degrees of freedom to represent the solution accurately. Adding polynomial enrichments improves dramatically the enrichment, but the solutions are still not as accurate as other solutions with the same polynomial degree that we will discuss shortly. The following curves show the results of using the first proposed enrichment for junctions (i.e., considering all subdomains with individual enrichments). It can be seen from the results that considering three enrichment functions gives more accurate results than using only two. This is in contrast to the results found in [11] for discontinuous displacement fields in polycrystalline materials, where $n - 1$ enrichments are used on a junction of n grains because one of the enrichments was linearly dependent. Here the functions within the grains are completely different among them so the solutions obtained considering n enrichments for an n -junction gives more accurate results. Finally, taking the ridge function proposed in [23] as the choice for interfaces, we use local junction enrichments. Once again we see that using a unique function to represent the junction does not perform as well as having individual enrichments, even though it requires less degrees of freedom. Convergence rates are not reported for this example because the reference energy has a finite accuracy. This reference value is accurate enough for the linear approximations, but it affects the rates for the quadratic ones.

5. Applications

This section presents two real applications where the proposed enrichment functions are used.

5.1. *Actively cooled microvascular material*

The goal of this example is to analyze a microvascular material with active cooling capabilities, thus using the proposed enrichments in a real problem. Much work has been done on the development of materials that mimic living organisms to provide self-healing and active cooling capabilities [42, 43, 44, 45]. For an active cooling microvascular material, thermal loads are applied and an embedded network containing a cooling fluid is used to reduce its maximum temperature. It can be shown (see reference [46]) that the equivalent heat sink generated by the fluid in a single microchannel is given by

$$q = \dot{m}c_f \frac{du}{dx'}, \quad (23)$$

where \dot{m} and c_f are the mass flow rate and specific heat of the fluid, respectively, and x' is the local coordinate in the direction of the channel. This simplified formulation for the *conjugated heat transfer* problem, whose assumptions lie outside the scope of this work, allows us to collapse the cooling effect of the fluid to a heat sink applied over the centerlines of the channels. The dependance of the heat sink on the temperature field implies that Equation (23) will contribute to the stiffness matrix in the finite element formulation. Of course, the accuracy in the representation of these sink terms is limited to the type of approximation used. In other words, the formulation above can represent a linear variation on the heat sink if a quadratic approximation is used. Furthermore, the stiffness matrix loses its symmetry due to the addition of these sink terms. The algorithm described in [10, 35] can still be used to solve the resulting system of equations with small changes.

Consider the mathematical model of a biomimetic active cooling material depicted in Figure 17. The material is composed of epoxy with thermal conductivity $\kappa = 0.3 \text{ W/mK}$. The material is represented by the rectangular domain Ω with sides $L_x = 66 \text{ mm}$ and $L_y = 68 \text{ mm}$. The microvascular cooling network, denoted as μVAC in the figure, contains microchannels that follow Murray's law [47]: At any junction,

$$\sum_i D_{pi}^3 = \sum_j D_{cj}^3,$$

where D_p and D_c denote the diameters of microchannels with inflow to and outflow from the junction, respectively. Murray's law ensures that the distribution of diameters in the network minimizes the pressure drop between the inlet and the outlet locations, given that the flow inside the microchannels is laminar. Innermost microchannels to the x barycentric axis have the smallest diameter $D = 200 \mu\text{m}$.

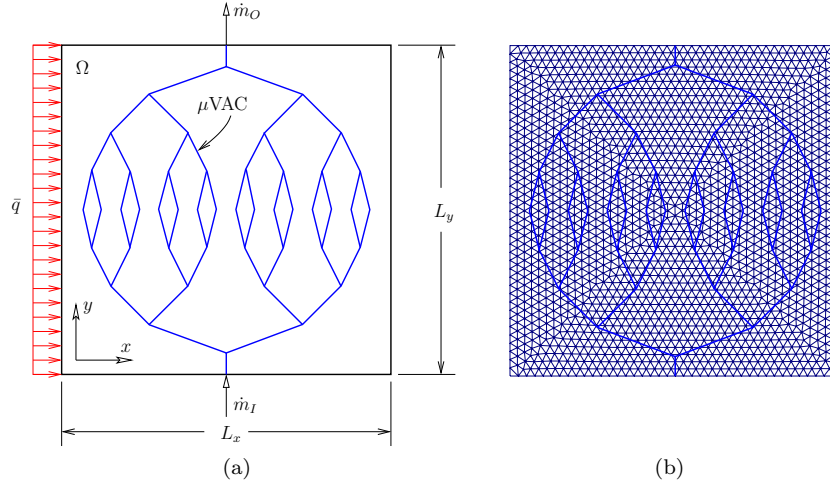


Figure 17: (a) Mathematical model of a biomimetic active cooling material composed of epoxy. The material has an embedded microvascular network with a distribution of diameter values that follows Murray's law. The domain contains a single inflow \dot{m}_I and a single outflow \dot{m}_O located on the bottom and top edges, respectively. A prescribed heat flux q is applied to the left edge whereas the remaining edges are convective boundaries. (b) Non-conforming finite element mesh used for the discretization.

To determine the pressure distribution in the network, the Hagen-Poiseuille law is used to represent the pressure drop in the i -th microchannel:

$$\Delta p_i = \frac{128\nu L_i}{\pi D_i^4} \dot{m}_i, \quad (24)$$

where L_i and D_i denote the length and diameter of the microchannel, respectively, and ν the kinematic viscosity of the fluid. Assembling the contribution of all microchannels in the network results in a linear system of equation $\vec{K}\vec{p} = \vec{c}$, where \vec{K} is the characteristic matrix

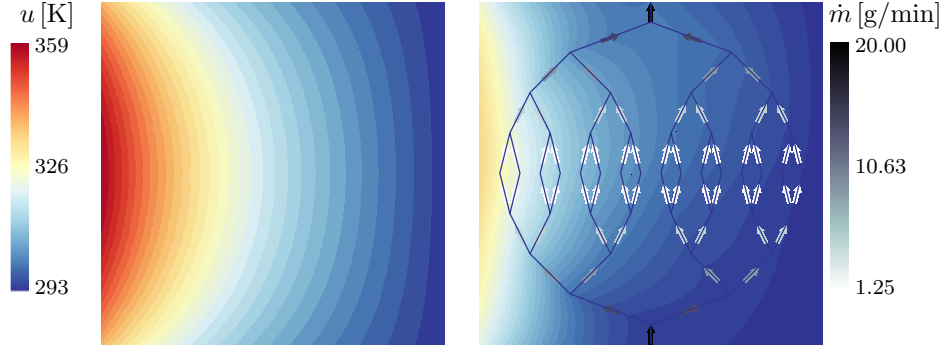


Figure 18: Temperature distribution for a biomimetic active cooling material with flow (right) and without it (left). The problem was solved on a non-conforming mesh using $\{1, \xi, \eta\} \times \{1, r_1\}$ as the set for interface enrichments and $\{1, \xi, \eta\} \times \{1, r_i\}_{i=1}^3$ for junction enrichments.

(the equivalent to the stiffness matrix in solid mechanics), \vec{p} is the pressure vector and \vec{c} is the consumption vector. The boundary conditions consist of a prescribed water mass inflow of 20 g/min and prescribed atmospheric pressure at the outflow.

The boundary value problem for the temperature solution has a prescribed heat flux $q = 500 \text{ W/m}$ on the left edge. The remaining edges have a convective boundary condition, with ambient temperature $u_\infty = 293 \text{ K}$. The right edge has a heat transfer coefficient $h_1 = 100 \text{ W/m}^2\text{K}$ whereas bottom and top edges have $h_2 = 10 \text{ W/m}^2\text{K}$.

The problem is then solved with a mesh that does not conform to the microvascular network (see Figure 17b) using $\{1, \xi, \eta\} \times \{1, r_1\}$ and $\{1, \xi, \eta\} \times \{r_i\}_{i=1}^3$ as the sets for interface and junction enrichments, respectively. The temperature distribution both considering the flow and neglecting it are illustrated in Figure 18 using the same scale. Injecting flow into the domain has the direct effect of reducing the temperature by about 25 K. Note that this formulation is able to capture the loss in symmetry with respect to the horizontal barycentric axis due to the fact that the fluid increases its temperature from the inlet to the outlet.

5.2. Polycrystalline microstructure example

Even though all the problems studied so far have focused on line heat sources (or heat sinks), the enrichment functions presented in this work can also be used to study problems containing material interfaces. Consider the polycrystalline microstructure on a square domain Ω shown in Figure 19. A square domain is used again and the grains inside it have increasing conductivity values (in W/mK) $\kappa_1 = 2$, $\kappa_2 = 4$, $\kappa_3 = 8$ and $\kappa_4 = 380$. A uniform heat flux $q = 100 \text{ W/m}$ is applied over the top edge. The bottom edge is a convective boundary, with ambient temperature $u_\infty = 293 \text{ K}$ and heat transfer coefficient $h = 100 \text{ W/m}^2\text{K}$. The problem is solved using the enrichment functions $\{1, \xi, \eta\} \times \{1, r_i\}_{i=1}^3$, resulting in a quadratic approximation. The resulting temperature distribution is presented in Figure 20, clearly demonstrating the ability of the proposed GFEM model to capture the discontinuous temperature gradients along the grain boundaries, including those at triple junctions.

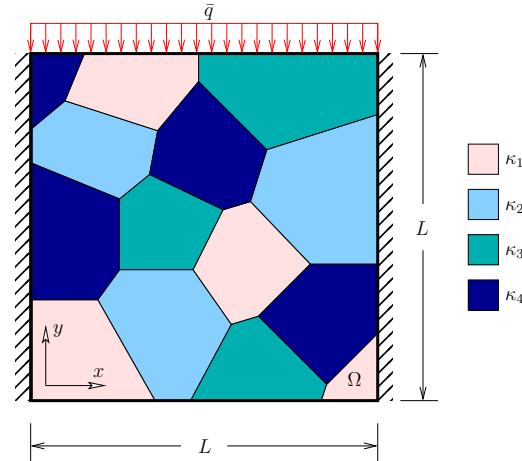


Figure 19: Schematic for the polycrystalline microstructure example. The material is divided in grains having different thermal conductivity values. Boundary conditions include insulated left and right edges, a constant heat flux q on the top edge and a convective boundary along the bottom edge.

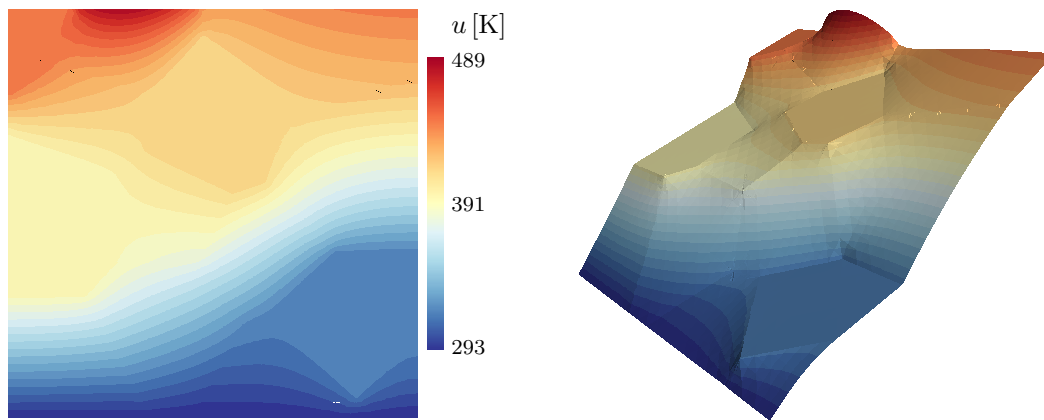


Figure 20: Temperature distribution for the polycrystalline microstructure example emphasizing the discontinuous gradients along grain boundaries.

6. Conclusions

The enrichments introduced in this work solve the problem of having multiple interfaces converging to a single point inside finite elements. When there is only a single interface, these enrichments reduce to the ramp enrichments discussed in detail in Sections 4.1 and 4.2. It was shown that the correction factor proposed by Fries in [28] is needed when ramp functions are used in a linear approximation. However, the ramp functions can only represent in this case a constant jump in the gradient of the field, so they fail to capture accurately the linear variation studied in Section 4.2 even when using the correction mentioned above. Also, the correction factor is not needed anymore when using a quadratic approximation and these functions recover optimal quadratic convergence rates.

It was shown that a single enrichment function (i.e., $R(\mathbf{x})$) for multiple interfaces does not recover optimal convergence rates. On the other hand, having one enrichment function per subdomain (i.e., $r_i(\mathbf{x})$) gives very accurate results. When the geometric representation of these subdomains is not available, junction enrichments can be built locally and used in conjunction with regular interface enrichments to provide more accurate results. It was shown in Section 4.3 that line bisectors have to be added because these enrichments are C^0 continuous along those lines as well. Adaptive integration can be used in the GFEM framework to find regions where the enrichment functions are not smooth. All results in this work reveal that quadratic approximations are more accurate than linear approximations for the same number of degrees of freedom.

Most examples studied in this work involved line heat sources in homogeneous materials to create the discontinuous gradient nature of the solution. The microvascular material example showed how this technique can be used in a real problem where the mesh is completely independent of the geometry of the network. The last example showed how the same enrichments can be used in heterogeneous materials. In this example the discontinuity in the gradient results from having different conductivity values across the grains in a polycrystalline microstructure. Even though the presented work has focused entirely on the solution of the Poisson equation, the extension to elasticity problems is straightforward, i.e., the enrichment functions presented are general and they should work in the context of other physical phenomena. Although likely, the applicability of the enrichment functions presented in this work to 3D problems with line or planar heat sources remains to be demonstrated.

ACKNOWLEDGEMENTS

A. M. Aragón and P. H. Geubelle gratefully acknowledge support from AFOSR (MURI grant number F49550-05-1-0346).

REFERENCES

1. Shipton LA. Thermal management applications for microvascular systems. Master's Thesis, University of Illinois at Urbana-Champaign 2007.
2. Sukumar N, Srolovitz DJ, Baker TJ, Prévost JH. Brittle fracture in polycrystalline microstructures with the extended finite element method. *International Journal for Numerical Methods in Engineering* 2003; **56**(14):2015–2037. URL <http://dx.doi.org/10.1002/nme.653>.

3. Duarte CA. The hp cloud method. PhD Thesis, The University of Texas at Austin, Austin, TX, USA December 1996.
4. Duarte CA, Oden JT. An h-p adaptive method using clouds. *Computer Methods in Applied Mechanics and Engineering* 1996; **139**(1-4):237–262. URL [http://dx.doi.org/10.1016/S0045-7825\(96\)01085-7](http://dx.doi.org/10.1016/S0045-7825(96)01085-7).
5. Duarte CA, Oden JT. H-p clouds – an h-p meshless method. *Numerical Methods for Partial Differential Equations* 1996; **12**(6):673–705. URL [http://dx.doi.org/10.1002/\(SICI\)1098-2426\(199611\)12:6<673::AID-NUM3>3.0.CO;2-P](http://dx.doi.org/10.1002/(SICI)1098-2426(199611)12:6<673::AID-NUM3>3.0.CO;2-P).
6. Oden JT, Duarte CAM, Zienkiewicz OC. A new cloud-based hp finite element method. *Computer Methods in Applied Mechanics and Engineering* 1998; **153**(1-2):117–126. URL [http://dx.doi.org/10.1016/S0045-7825\(97\)00039-X](http://dx.doi.org/10.1016/S0045-7825(97)00039-X).
7. Melenk JM, Babuška I. The partition of unity finite element method: Basic theory and applications. *Computer Methods in Applied Mechanics and Engineering* 1996; **139**(1-4):289–314. URL [http://dx.doi.org/10.1016/S0045-7825\(96\)01087-0](http://dx.doi.org/10.1016/S0045-7825(96)01087-0).
8. Babuška I, Melenk JM. The partition of unity method. *International Journal for Numerical Methods in Engineering* 1997; **40**(4):727–758. URL [http://dx.doi.org/10.1002/\(SICI\)1097-0207\(19970228\)40:4<727::AID-NME86>3.0.CO;2-N](http://dx.doi.org/10.1002/(SICI)1097-0207(19970228)40:4<727::AID-NME86>3.0.CO;2-N).
9. Belytschko T, Gracie R, Ventura G. A review of extended/generalized finite element methods for material modeling. *Modelling and Simulation in Materials Science and Engineering* 2009; **17**(4):043001 (24pp). URL <http://stacks.iop.org/0965-0393/17/043001>.
10. Duarte CA, Babuška I, Oden JT. Generalized finite element methods for three-dimensional structural mechanics problems. *Computers & Structures* 2000; **77**(2):215–232. URL [http://dx.doi.org/10.1016/S0045-7949\(99\)00211-4](http://dx.doi.org/10.1016/S0045-7949(99)00211-4).
11. Simone A, Duarte CA, Van der Giessen E. A generalized finite element method for polycrystals with discontinuous grain boundaries. *International Journal for Numerical Methods in Engineering* 2006; **67**(8):1122–1145. URL <http://dx.doi.org/10.1002/nme.1658>.
12. Belytschko T, Black T. Elastic crack growth in finite elements with minimal remeshing. *International Journal for Numerical Methods in Engineering* 1999; **45**(5):601–620. URL [http://dx.doi.org/10.1002/\(SICI\)1097-0207\(19990620\)45:5<601::AID-NME598>3.0.CO;2-S](http://dx.doi.org/10.1002/(SICI)1097-0207(19990620)45:5<601::AID-NME598>3.0.CO;2-S).
13. Moës N, Dolbow J, Belytschko T. A finite element method for crack growth without remeshing. *International Journal for Numerical Methods in Engineering* 1999; **46**(1):131–150. URL [http://dx.doi.org/10.1002/\(SICI\)1097-0207\(19990910\)46:1<131::AID-NME726>3.0.CO;2-J](http://dx.doi.org/10.1002/(SICI)1097-0207(19990910)46:1<131::AID-NME726>3.0.CO;2-J).
14. Daux C, Moës N, Dolbow J, Sukumar N, Belytschko T. Arbitrary branched and intersecting cracks with the extended finite element method. *International Journal for Numerical Methods in Engineering* 2000; **48**(12):1741–1760. URL [http://dx.doi.org/10.1002/1097-0207\(20000830\)48:12<1741::AID-NME956>3.0.CO;2-L](http://dx.doi.org/10.1002/1097-0207(20000830)48:12<1741::AID-NME956>3.0.CO;2-L).
15. Duarte CA, Hamzeh ON, Lyszka TJ, Tworzydło WW. A generalized finite element method for the simulation of three-dimensional dynamic crack propagation. *Computer Methods in Applied Mechanics and Engineering* 2001; **190**(15-17):2227–2262. URL [http://dx.doi.org/10.1016/S0045-7825\(00\)00233-4](http://dx.doi.org/10.1016/S0045-7825(00)00233-4).
16. Chahine E, Laborde P, Renard Y. A quasi-optimal convergence result for fracture mechanics with xfem. *Comptes Rendus Mathématique* 4 2006/4/1; **342**(7):527–532. URL <http://dx.doi.org/10.1016/j.crma.2006.02.002>.
17. Merle R, Dolbow J. Solving thermal and phase change problems with the extended finite element method. *Computational Mechanics* 2002; **28**(5):339–350. URL <http://dx.doi.org/10.1007/s00466-002-0298-y>.
18. Dolbow J, Fried E, Ji H. Chemically induced swelling of hydrogels. *Journal of the Mechanics and Physics of Solids* 2004/1; **52**(1):51–84. URL [http://dx.doi.org/10.1016/S0022-5096\(03\)00091-7](http://dx.doi.org/10.1016/S0022-5096(03)00091-7).
19. Dolbow J, Fried E, Ji H. A numerical strategy for investigating the kinetic response of stimulus-responsive hydrogels. *Computer Methods in Applied Mechanics and Engineering* 10 2005/10/15; **194**(42-44):4447–4480. URL <http://dx.doi.org/10.1016/j.cma.2004.12.004>.
20. Ji H, Mourad H, Fried E, Dolbow J. Kinetics of thermally induced swelling of hydrogels. *International Journal of Solids and Structures* 2006/4; **43**(7-8):1878–1907. URL <http://dx.doi.org/10.1016/j.ijsolstr.2005.03.031>.
21. Strouboulis T, Copps K, Babuška I. The generalized finite element method. *Computer Methods in Applied Mechanics and Engineering* 2001; **190**(32-33):4081–4193. URL [http://dx.doi.org/10.1016/S0045-7825\(01\)00188-8](http://dx.doi.org/10.1016/S0045-7825(01)00188-8).
22. Sukumar N, Chopp DL, Moës N, Belytschko T. Modeling holes and inclusions by level sets in the extended finite-element method. *Computer Methods in Applied Mechanics and Engineering* 2001; **190**(46-47):6183–6200. URL [http://dx.doi.org/10.1016/S0045-7825\(01\)00215-8](http://dx.doi.org/10.1016/S0045-7825(01)00215-8).
23. Moës N, Cloirec M, Cartraud P, Remacle JF. A computational approach to handle complex microstructure geometries. *Computer Methods in Applied Mechanics and Engineering* 2003; **192**(28-30):3163–3177. URL [http://dx.doi.org/10.1016/S0045-7825\(03\)00346-3](http://dx.doi.org/10.1016/S0045-7825(03)00346-3).
24. Babuška I, Osborn JE. Generalized finite element methods: Their performance and their relation to mixed

- methods. *SIAM Journal on Numerical Analysis* Jun, 1983; **20**(3):510–536. URL <http://www.jstor.org/stable/2157269>.
25. Srinivasan KR, Matouš K, Geubelle PH. Generalized finite element method for modeling nearly incompressible bimaterial hyperelastic solids. *Computer Methods in Applied Mechanics and Engineering* 2008; URL <http://dx.doi.org/10.1016/j.cma.2008.07.014>.
 26. Belytschko T, Möes N, Usui S, Parimi C. Arbitrary discontinuities in finite elements. *International Journal for Numerical Methods in Engineering* 2001; **50**(4):993–1013. URL [http://dx.doi.org/10.1002/1097-0207\(20010210\)50:4<993::AID-NME164>3.0.CO;2-M](http://dx.doi.org/10.1002/1097-0207(20010210)50:4<993::AID-NME164>3.0.CO;2-M).
 27. Robbins J, Voth TE. An extended finite element formulation for modeling the response of polycrystalline materials to shock loading. *American Physical Society, 15th APS Topical Conference on Shock Compression of Condensed Matter*, 2007.
 28. Fries TP. A corrected xfm approximation without problems in blending elements. *International Journal for Numerical Methods in Engineering* 2008; **75**(5):503–532. URL <http://dx.doi.org/10.1002/nme.2259>.
 29. Möes N, Béchet E, Tourbier M. Imposing dirichlet boundary conditions in the extended finite element method. *International Journal for Numerical Methods in Engineering* 2006; **67**(12):1641–1669. URL <http://dx.doi.org/10.1002/nme.1675>.
 30. Babuška I, Banerjee U, JE O. Survey of meshless and generalized finite element methods: A unified approach. *Acta Numerica* 2003; **12**:1–125.
 31. Chessa J, Wang H, Belytschko T. On the construction of blending elements for local partition of unity enriched finite elements. *International Journal for Numerical Methods in Engineering* 2003; **57**(7):1015–1038. URL <http://dx.doi.org/10.1002/nme.777>.
 32. Ventura G, Gracie R, Belytschko T. Fast integration and weight function blending in the extended finite element method. *International Journal for Numerical Methods in Engineering* 2009; **77**(1):1–29. URL <http://dx.doi.org/10.1002/nme.2387>.
 33. Tarancón JE, Vercher A, Giner E, Fuenmayor FJ. Enhanced blending elements for xfm applied to linear elastic fracture mechanics. *International Journal for Numerical Methods in Engineering* 2009; **77**(1):126–148. URL <http://dx.doi.org/10.1002/nme.2402>.
 34. Gracie R, Wang H, Belytschko T. Blending in the extended finite element method by discontinuous galerkin and assumed strain methods. *International Journal for Numerical Methods in Engineering* 2008; **74**(11):1645–1669. URL <http://dx.doi.org/10.1002/nme.2217>.
 35. Strouboulis T, Babuška I, Copps K. The design and analysis of the generalized finite element method. *Computer Methods in Applied Mechanics and Engineering* 1 2000; **181**(1-3):43–69. URL [http://dx.doi.org/10.1016/S0045-7825\(99\)00072-9](http://dx.doi.org/10.1016/S0045-7825(99)00072-9).
 36. Osher SJ, Fedkiw RP. *Level Set Methods and Dynamic Implicit Surfaces*. 1st. edn., Springer, 2002.
 37. Duarte CA, Reno LG, Simone A. A high-order generalized fem for through-the-thickness branched cracks. *International Journal for Numerical Methods in Engineering* 2007; **72**(3):325–351. URL <http://dx.doi.org/10.1002/nme.2012>.
 38. Pereira JP, Duarte CA, Guoy D, Jiao X. hp-generalized fem and crack surface representation for non-planar 3-d cracks. *International Journal for Numerical Methods in Engineering* 2009; **77**(5):601–633. URL <http://dx.doi.org/10.1002/nme.2419>.
 39. Chessa J, Smolinski P, Belytschko T. The extended finite element method (xfem) for solidification problems. *International Journal for Numerical Methods in Engineering* 2002; **53**(8):1959–1977. URL <http://dx.doi.org/10.1002/nme.386>.
 40. Vaughan B, Smith B, Chopp D. A comparison of the extended finite element method with the immersed interface method for elliptic equations with discontinuous coefficients and singular sources. *Communications in Applied Mathematics and Computational Science* 2006; **1**(1):207–228.
 41. Strouboulis T, Copps K, Babuška I. The generalized finite element method: an example of its implementation and illustration of its performance. *International Journal for Numerical Methods in Engineering* 2000; **47**(8):1401–1417. URL [http://dx.doi.org/10.1002/\(SICI\)1097-0207\(20000320\)47:8<1401::AID-NME835>3.0.CO;2-8](http://dx.doi.org/10.1002/(SICI)1097-0207(20000320)47:8<1401::AID-NME835>3.0.CO;2-8).
 42. White SR, Sottos NR, Geubelle PH, Moore JS, Kessler MR, Sriram SR, Brown EN, Viswanathan S. Autonomic healing of polymer composites. *Nature* 2001; **409**:794–797.
 43. Toohey KS, Sottos NR, Lewis JA, Moore JS, White SR. Self-healing materials with microvascular networks. *Nature Materials* June 2007; **6**:581–585.
 44. Aragón AM, Hansen CJ, Wu W, Geubelle PH, Lewis JA, White SR. Computational design and optimization of a biomimetic self-healing/cooling material. *Proceedings of SPIE*, vol. 6526, 2007.
 45. Aragón AM, Wayer JK, Geubelle PH, Goldberg DE, White SR. Design of microvascular flow networks using multi-objective genetic algorithms. *Computer Methods in Applied Mechanics and Engineering* 2008; **197**(49-50):4399–4410. URL <http://dx.doi.org/10.1016/j.cma.2008.05.025>.
 46. Kays WM, Crawford ME, Weigand B. *Convective heat and mass transfer*. 4th edn., McGraw-Hill, 2004.
 47. Murray CD. The physiological principle of minimum work. i. the vascular system and cost of blood volume.

Proceedings of the National Academy of Sciences of the United States of America 1926; **12**(3):207–214.
URL <http://www.pnas.org/content/12/3/207.short>.